Solid Freeform Fabrication 2024: Proceedings of the 35th Annual International Solid Freeform Fabrication Symposium – An Additive Manufacturing Conference
Reviewed Paper

Exploring Effects of Part Size for Laser Powder Bed Fusion Manufactured Bismuth Telluride using In-Situ Thermal Tomography

Clayton Perbix[*], Saniya LeBlanc[†], Joe Walker[‡], and Joy Gockel[*]

[*]Colorado School of Mines, Golden, CO 80401
[†]George Washington University, Washington, D.C. 20052
[‡]Open Additive, Beavercreek, OH 45440

Abstract

Bismuth telluride (Bi_2Te_3) is an important material used in thermoelectric applications. However, the effect on microstructure and ultimately thermoelectric performance when it is additively manufactured using laser powder bed fusion (PBF-LB) is not well understood. This study investigates the effect of various processing parameters and part geometries on the quality and microstructure of PBF-LB bismuth telluride parts. In-situ process monitoring was performed using thermal tomography imaging to provide information about sample thermal behavior. Results showed that increasing part size led to undesirable printing defects, and individual parts exhibited a broad range of microstructural features. Thermal tomography data showed that larger layer cross-sections retained more heat during processing, a result contradictory to what has been shown in structural metals processing. Furthering our understanding of the effect of part geometry during PBF-LB manufacturing will improve our ability to create more complex structures, and enable higher performance thermoelectric devices.

Introduction

Bismuth telluride (Bi_2Te_3) is a commonly employed semiconductor material in the field of thermoelectrics, used for both cooling and power generation applications. Its exceptional thermoelectric properties stem from its high thermoelectric figure of merit (ZT), particularly around room temperature [1]. The high ZT is attributed to its advantageous material properties, including high band degeneracy, high carrier mobility, and relatively low thermal conductivity [2], [3]. Bismuth telluride can serve as the base material for both n-type and p-type thermoelectric components depending on atomic composition. Dopants can also be included such as selenium for n-type, and antimony for p-type, which have demonstrated improved thermoelectric properties in specific applications [4].

Current manufacturing of bismuth telluride thermoelectric devices involves techniques such as spark plasma sintering, zone refining, and mechanical alloying [5]. These methods allow for precise control over the material's microstructure, resulting in high quality, uniformly dense parts [6]. However, the available fabrication geometries are limited and require sectioning of the bulk material, which produces significant waste. Additive manufacturing (AM) provides the ability to quickly fabricate complex geometries with minimal material waste. AM of bismuth telluride is currently being pursued with a variety of technologies, including laser powder bed fusion (PBF-LB), direct ink writing [7], modified vat photopolymerization [8], and other hybrid AM methods [9], [10], [11].

PBF-LB is an advanced AM technology where a high-powered laser selectively melts and fuses layers of powder to create complex three-dimensional objects, leveraging precise control over the process parameters and local thermal environment to produce parts with high geometric accuracy and tailored microstructures [12]. Some advantages of the technique include net-shape and in-device fabrication, which simplifies manufacturing. It enables unique and traditionally impossible part geometries, which have the potential to produce thermoelectrically beneficial shapes [13], tailored lattices [14], and conformal parts. The PBF-LB process also allows for creation of unique and traditionally impossible alloys, as well as microstructure control including grain textures, metastable phases, and spatially changing properties [15], [16], [17], [18], [19].

Part creation via PBF-LB also presents a new set of manufacturing challenges. To the first approximation, PBF-LB processes will create the equivalent of multiple miles of weld bead per cubic inch of material. This allows for extremely discreet material addition, but the highly localized and non-equilibrium environment that exists for each length of weld can induce unwanted variability in the finished part. PBF-LB material solidification is an extremely dynamic event, affected in part by intrinsic material properties, localized environmental changes, and process parameter selection. The ability to confidently account for all these variations in real time through in-situ monitoring should allow the process to more accurately control the chosen material properties during the manufacturing process.

This study aims to investigate the effects of printed part size and shape on manufacturing quality and microstructure of bismuth telluride parts fabricated with PBF-LB. The focus is on understanding the relationship between part geometry (both layer cross-section and height above the build plate), energy input, thermal tomography output, and resulting part print quality.

Methods

Materials and Sample Production:

Neat bismuth telluride powder was used for all experiments, purchased from Alfa Aesar. The powder ordered from the supplier came with a wide range of different particle sizes and required further preparation before printing. To prepare the powder for printing it needed to be sieved to a range of 20-75 μm based on previous experience for spreading [20]. Hand sieving was performed. To increase the yield, a pestle was used, with the coarse sieve acting as the mortar. The bismuth telluride powder is very brittle so it could be lightly ground into the sieve with the pestle and broken into particles within the desired range.

Bismuth telluride presents a few processing challenges, as it has an uncommon set of material properties compared to most PBF-LB materials, including a low melting point (585 °C) and low thermal conductivity (~1 W/m·K) [3]. Additionally, the powder's non-uniform and jagged bulk morphology makes it difficult to spread (Figure 1, left), further necessitating the use of a custom printer, which was built and operated by Open Additive (Figure 1, right). The system includes a fully inert environment, counter-rotating roller re-coater to spread and compact the irregular powder, and a 50 mm circular build plate made from stainless steel. The system is outfitted with a 1000 W, 1064 nm, ytterbium laser produced by IPG Photonics. The printer is also

equipped with a series of in-situ process monitoring sensors. This experiment focused on the thermal tomography output, generated by a 12 MP long exposure CMOS NIR camera, which produced a single thermal response image per scan. This is done by setting the exposure time equal to the frame rate, and then integrating the frames together into a single image after each layer is complete. The tomography sensor was chosen because it is directly correlated to temperature, which is relevant to solidification conditions and resultant microstructure. It is also readily available in commercial machines today and has simple data output.

Figure 1: SEM image of coarse and irregular bismuth telluride powder (left). Open Additive's custom bismuth telluride PBF-LB machine (right).

Experimental Design:

Parts with varying geometries were designed to explore the influence of changes in cross-sectional area (XY), as well as height above the build plate (Z). Samples were printed with small (3x3 mm) and large (10x10 mm) XY cross-sections, as well as a pyramid shape that sweeps from a 15x15 mm base up to a point (Figure 2). The small parts are equivalent to the controls, but upright, and were printed with touching corners to improve print performance and avoid build plate delamination. Control samples are also shown in Figure 2, printed to match the geometry of previous experiments to allow for direct comparison [20]. The new sample geometries were printed taller and wider to observe the effect of thermal buildup in the parts as they grow further from the build plate, as well as potential changes in the thermal tomography based on the part's print cross-section.

Print parameters were chosen based on prior successful experiments in an attempt to ensure high quality parts [20]. A narrow range of parameters were selected to remain near peak performance, while still providing some parameter variability to enhance the experiment's breadth. The samples were printed in sets of four, varying power and hatch spacing to produce these scenarios: 18 W/38 µm, 22 W/38 µm, 18 W/25 µm, 22 W/25 µm. All other print parameters were held constant, including scan speed of 500 mm/s, layer thickness of 150 µm, no contours, no burn passes, and a distinct double hatch scan strategy—each layer was scanned twice by the laser in the

same hatch orientation before recoating, (e.g. 0°, 0°, recoat, 90°, 90°, recoat, 180°, 180°, recoat, 270°, 270°, recoat, repeat). The new parts were designed with square print cross-sections, which, in concert with the scan strategy, allowed for each layer to have the same basic scan pattern (albeit rotated a quarter turn each time). Simplifying the scan pattern means the samples are effectively four-fold rotationally symmetric, which provides a more consistent thermal environment from one layer to the next, and further simplifies the analysis as the XZ and YZ planes are equivalent.

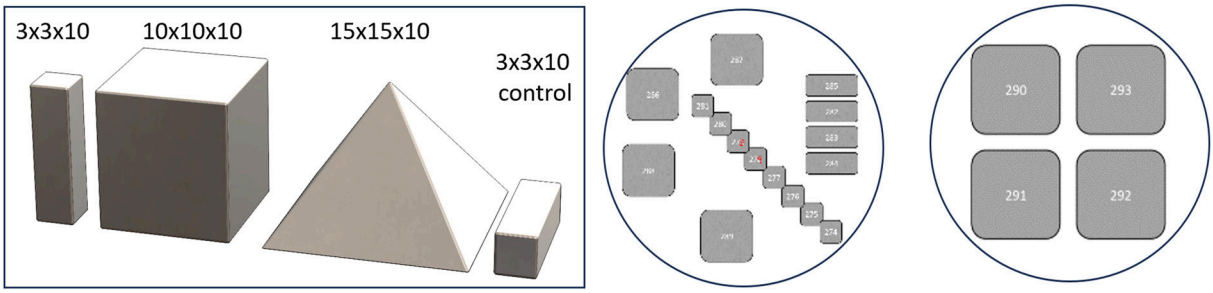

Figure 2: Experimental setup, part shapes in mm (left), and build locations for each print (right).

Sample Preparation:

Samples were received from Open Additive, documented, and then cast into epoxy molds using Buehler Epofix. The larger specimens were cross sectioned through the approximate center, in either the XZ or YZ planes. Cuts were made with an Allied TechCut5x using a diamond saw, 3000 rpm, feed 10 mm/min, with flood coolant. The smaller specimens were mounted directly and sanded down to their midpoints. All samples were then polished using a Struers LaboForce-100 counter-rotating auto polisher according to the procedure dictated in Table 1.

Table 1: Bismuth telluride auto-polishing procedure.

Grit (µm)	Type	Lubricant	Time (s)	Normal Force (N)	Disk RPM	Part RPM
15	Diamond lap film	Water	600*	20	80	50
9	Diamond lap film	Water	60	10	80	50
6	Diamond suspension on fabric nap	Glycol	60	10	80	50
3	Diamond suspension on fabric nap	Glycol	60	10	80	50
1	Diamond suspension on fabric nap	Glycol	60	10	80	50
.05	Colloidal silica on fabric nap	Water	30	10	80	50

**Depending on how much material needed to be removed to reach approximate center cross-section of part*

Microscopy:

Various analysis tools were used to qualitatively evaluate the printed samples. Visible light microscopy was performed using a Keyence VHX5000 under confocal illumination and cross-polarization. Images were captured at 200x optical magnification using the software-based automatic montage to capture larger areas. Cross polarizer orientation was chosen to maximize DIC visual contrast. Scanning electron microscopy was performed using an FEI Quanta 200 ESEM with an electron backscatter detector. Note the brightness and contrast of captured SEM images are not quantitative, but care was taken to match them between samples.

Results

Initial Observations:

The printed parts exhibited varying degrees of internal cohesion, external surface finishes, and dimensional accuracy. The build plate zone exhibited several issues, including warping, corner lift-off, rounded edges, and surface irregularities. These distortions can primarily be attributed to internal thermal stresses and inadequate adhesion to the build plate. The surface roughness was orientation dependent, where down-skins that touched the build plate were mostly smooth, the side-skins displayed thin horizontal layers (typical of PBF-LB), but the top-skins exhibited various sizes of an unexpectedly bulbous surface.

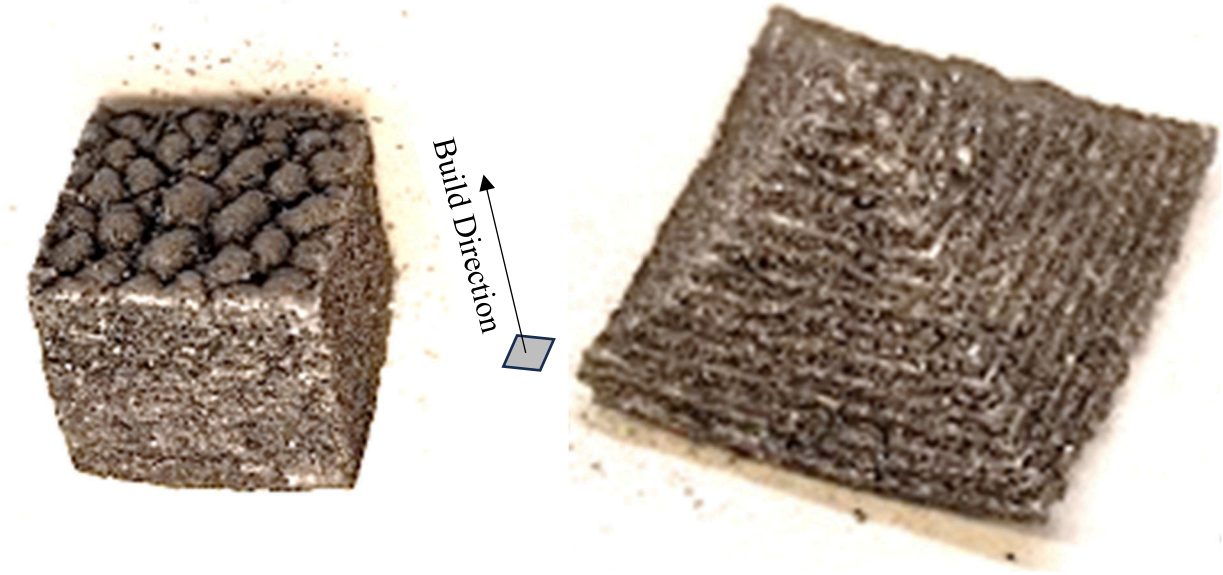

Figure 3: Example samples as received: 10mm cube (left), and pyramid with 15mm base (right).

The poor-quality top surfaces appear to be the result of unforeseen macroscopic columns that grew pervasively throughout the larger parts, including the pyramids. Some of the smaller 3 mm pillars showed signs of columns as well, with part examples shown in the cross-section images in Figure 4. The control samples (3 mm in height) did not show signs of columns, likely due to columns only beginning after the base region, starting approximately 3 mm from the build plate. Further investigation into these structures is necessary to understand their formation mechanisms, and ultimately how to avoid them. It is also worth noting that the samples exhibited a large amount of porosity. The porosity level in these samples was higher than previous samples printed under, theoretically, the same processing conditions. Further work is also required to determine the source of this porosity.

Another notable observation was the formation of distinct morphological regions within all the parts, identified here as the base, bulk, and top regions. Figure 4 shows example parts exhibiting the various regions, along with accompanying visual legends. These features are commonly seen in PBF-LB parts, as the local thermal environment is particularly potent at affecting solidification behavior. In these prints, being near the steel build plate, the unfused powder, the surface gas flow, or other portions of the sample itself, can each act like distinct thermal environments with distinct solidification results.

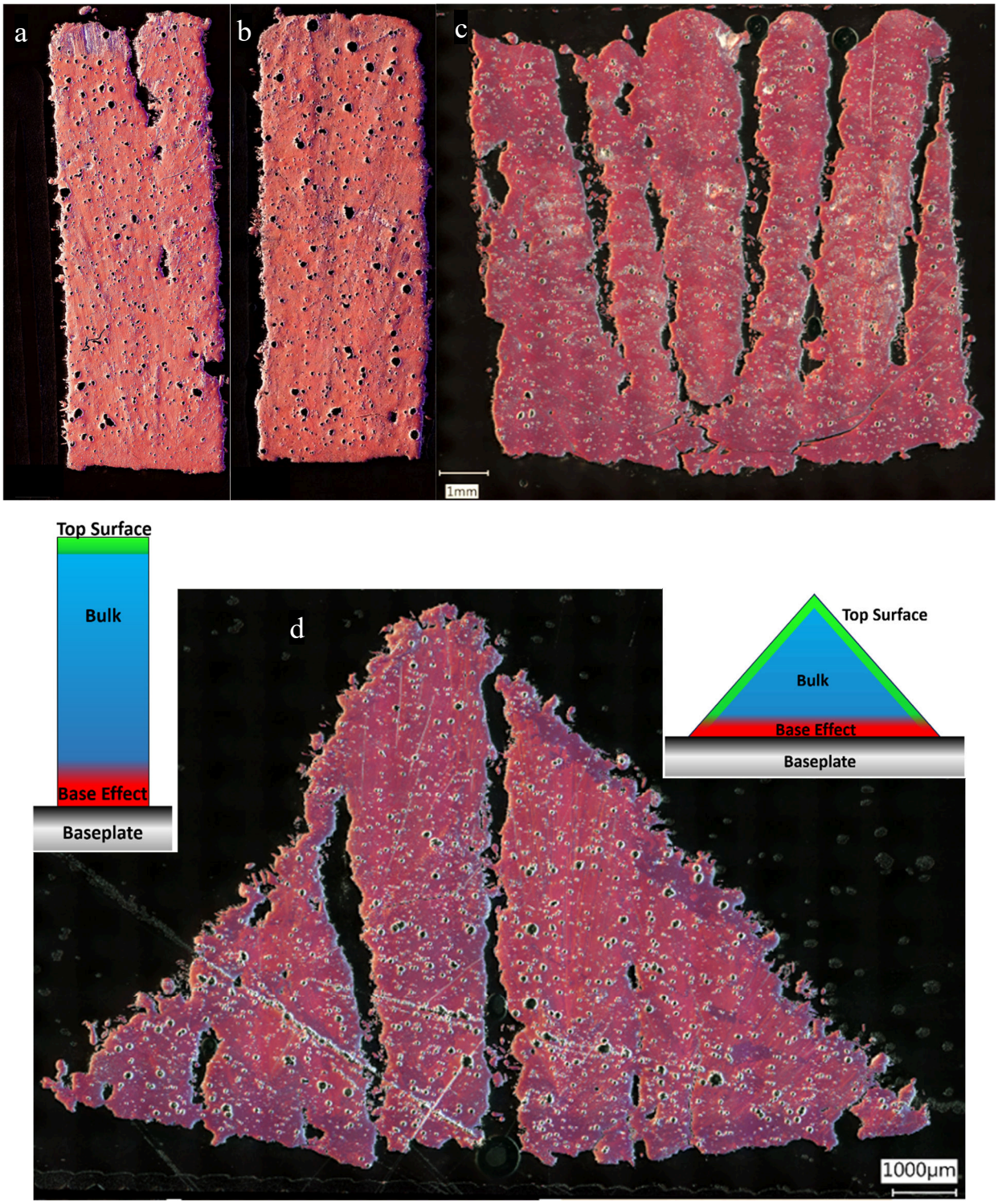

Figure 4: Cross-polarized microscopy images of part midsections of typical sample outcomes: two of the narrow 3 mm columns (a and b), a 10 mm cube (c), and a pyramid (d), along with accompanying build zone legends. Visible in these images are examples of sample warping, cracking, distinct morphological zones, macro-columns, polishing artifacts, and various sizes and forms of porosity.

Microstructure:

Microstructural investigation of the parts revealed significant variability influenced by part geometry, as well as local effects based on location within the part. It was generally observed that smaller parts exhibited more uniform feature orientations and fewer defects, while larger parts showed more significant atomic segregation and more random orientations. This difference likely results from the steeper and more uniformly upward thermal gradient in the smaller parts compared to the large cross-sections that allow heat to spread laterally.

Base Effect Region:

The base effect region in all samples showed the finest and most homogenous microstructures, with weak trends in feature orientation and elongation. The larger parts did exhibit more horizontal microstructure features, suggesting a more horizontal alignment of the thermal gradient during solidification. This region was unpredictable and varied considerably, highlighting the complex thermal dynamics at play during the initial stages where the build plate strongly affects heat flow.

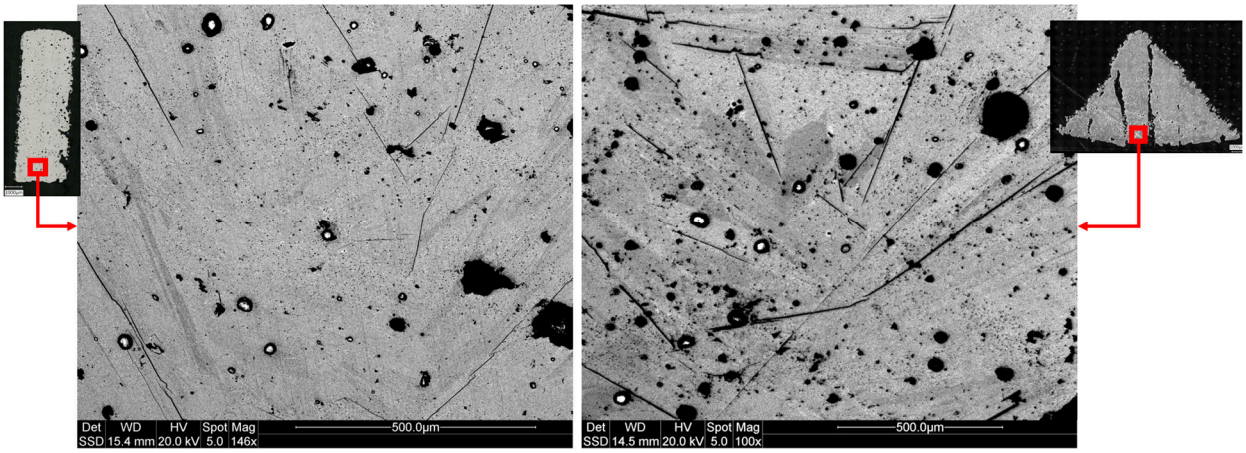

Figure 5: SEM image comparison of base effect regions in a small part (left) and a large part (right). The inset images show approximately where in each sample the images were taken.

Bulk Region:

The majority of the bulk region was characterized by small, randomly aligned domains in both small and large parts, although the larger samples exhibited higher inter-dendritic segregation (Figure 6). The slightly larger and more segregated microstructure in the bigger part suggest the cooling was comparatively slower overall. As the parts grow taller, the bulk zones tend towards vertically oriented features, which can be seen in the bottom portion of the images in Figure 7.

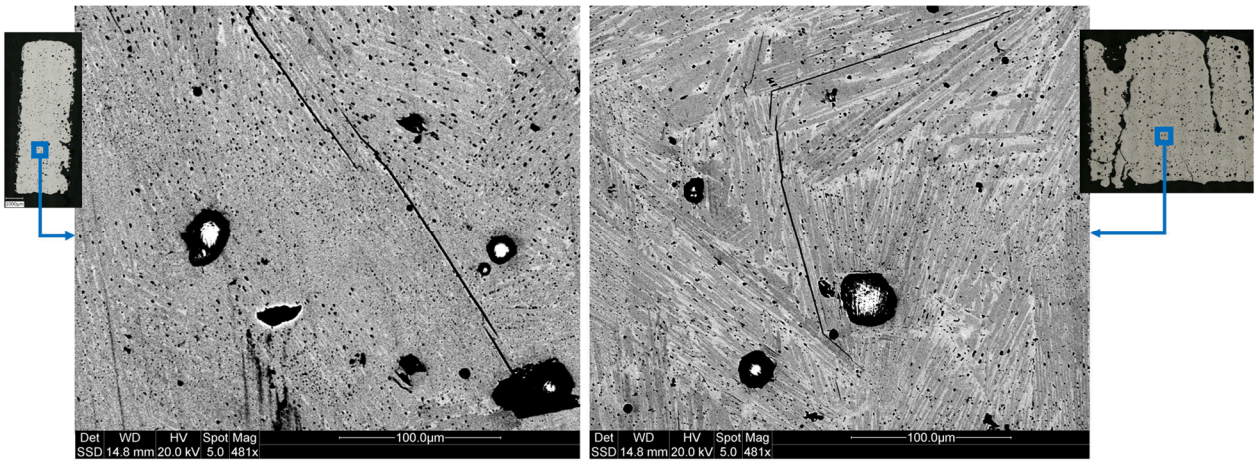

Figure 6: SEM images comparing the bulk regions of a 3 mm column (left) and 10 mm cube (right). The inset images show approximately where in each sample the images were taken.

Top Region:

The top region of all parts displayed similar characteristic vertical dendritic growth with narrow feature spacing, along with an increase in the black speckling. The speckling is likely elemental micro-segregation in the interdendritic regions during cooling. Such observations suggest extremely fast solidification of the material as it is initially deposited at the surface. These phenomena will only remain on topmost surfaces though, as the bulk below is clearly different, showing that feature coarsening must be occurring during later passes due to remelting and potentially solid-state transformations.

While this experiment did not necessarily demonstrate control of the microstructure creation process, it was clear that changing part geometry does have an effect on the creation process. These findings underscore the importance of carefully optimizing printing parameters and understanding the thermal environment in the PBF-LB process to achieve desired microstructural properties.

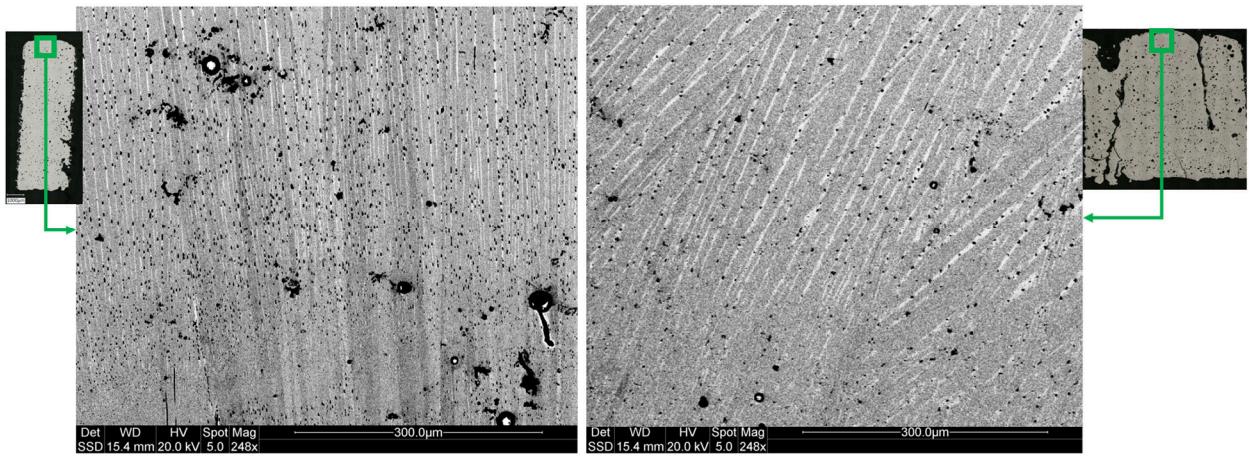

Figure 7: SEM imaging comparison of part's top region microstructure, 3 mm column (left) and 10 mm cube (right). The inset images show approximately where in each sample the images were taken.

Thermal Tomography Imaging:

Thermal tomography data were provided from Open Additive as per-layer images of the build area, where each pixel represented the integral sum of its brightness over the duration of the layer being printed. With these image arrays, a MATLAB script was written to parse each part individually within the tomography image. Each isolated part would then provide an average and standard deviation of its brightness for each scan. The 8-step cycle of the chosen laser scanning strategy caused a systemic cycle in the data, as the orientation of the laser path in relation to the off-axis tomography camera induced large brightness variations per layer in what was otherwise a uniform thermal environment. To account for this systemic error, an 8-point sliding average filter was applied in later analysis.

Visual examination of the data was a valuable initial step in the analysis process, providing insights into underlying patterns and anomalies. Figure 8 presents tomography images captured during the first laser scan, showing inconsistent thermal signatures due to previous prints on the reused build plate. Despite those inconsistencies, there are still part-to-part brightness variations visible, dependent on the selected print parameters. Figure 9 shows each of the four 10 mm cubes at approximately 8 mm build height, where macroscopic columns are clearly visible and unchanging. The column widths trend smaller as heat input is reduced, which can be seen as the reduction in sample brightness. This phenomenon appears similar to other examples of convective thin liquid layers, as seen in Benard-Marangoni flow [21]. Although the material does not remain liquid for long, this suggests that the entire top surface is repeatedly made molten, and convective. Other bright spots in the tomography images are likely indicative of stochastic events, such as spatter, that can lead to additional defects in the parts.

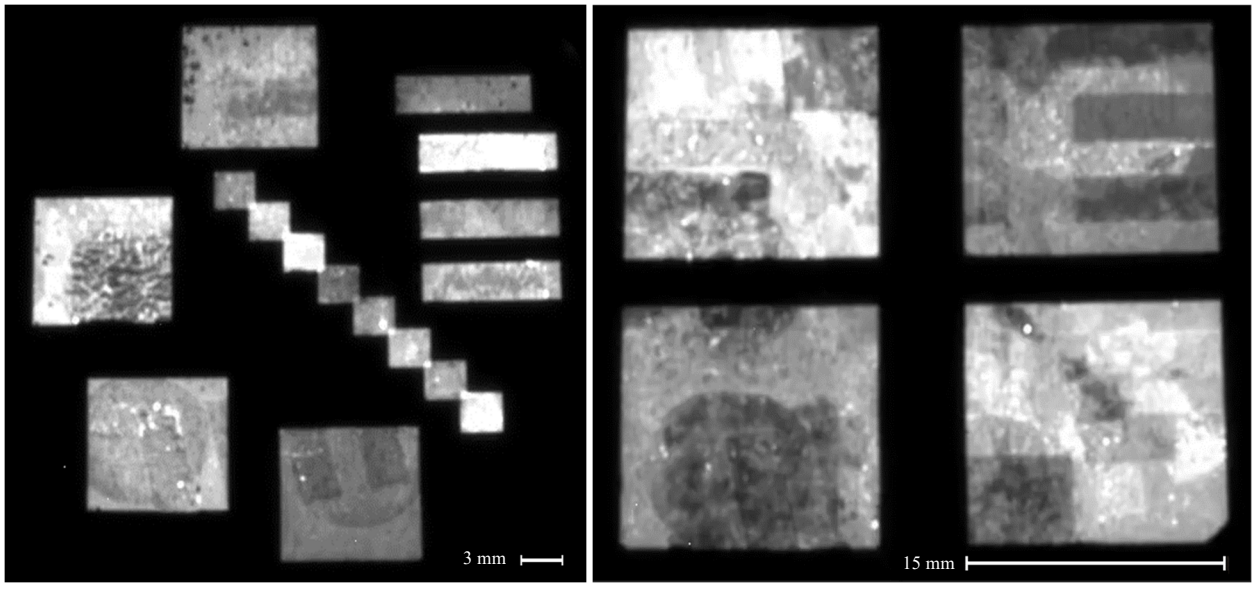

Figure 8: Tomography images, captured at scan 1, showing all printed samples used in the experiment. The smaller parts are shown on the left, while the pyramids are on the right. Brightness variations are visible due to parameter selection, as well as some startup anomalies.

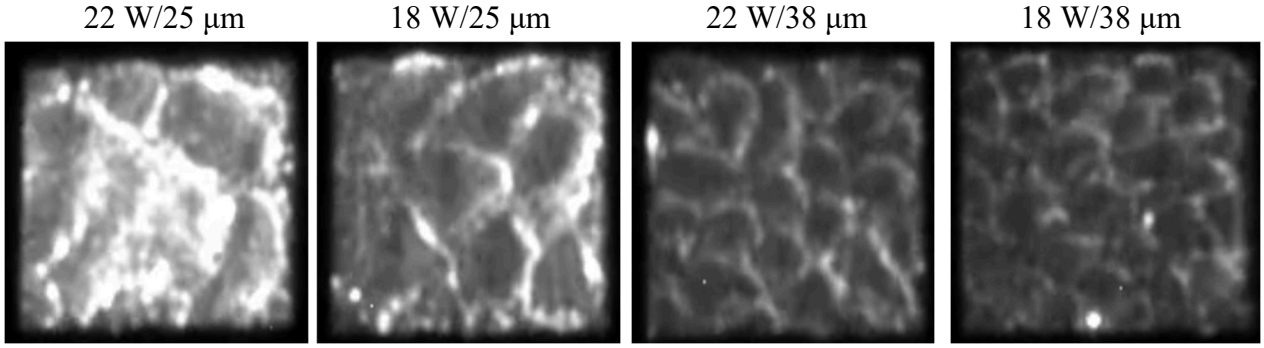

Figure 9: Array of 10 mm cubes at approximately steady state, showing the trend in both tomography brightness, and column size. Labels: laser power / hatch spacing.

An unabridged array of the tomography data for a single cube is presented in Figure 10. The montage shows similar characteristic patterns to those observed across the other prints, including the 8-cycle brightness pattern repeated across each row, the initial brightness dip then spike, and the steady state region after. Other qualitative aspects of the print process are evident in the tomography images as well, including the onset and continuation of the macroscopic column formation, and part delamination from the build plate. Although tomography captures images of emissions from the top surface as the build progresses, it does not directly identify the unique microstructural features that remain on top surfaces.

The initial dip in tomography sensor output in the base effect zone reflects the variable thermal contact of parts with the build plate. This can be attributed to the different print parameters used, as well as effects of previous builds causing different amounts of part adhesion. The dip recovery through the transition to the bulk region occurs due to increasing thermal insulation. As parts grow further from the build plate, heat conduction from top to bottom becomes throttled enough that heat begins to build up in the part, which is common in PBF-LB. Improving thermal coupling between the build plate and the printed part can help mitigate these issues. Techniques such as preheating the build plate, using a thermal interface material, or implementing initial ‘burn pass’ layers with modified parameters, have potential to enhance thermal contact and improve quality.

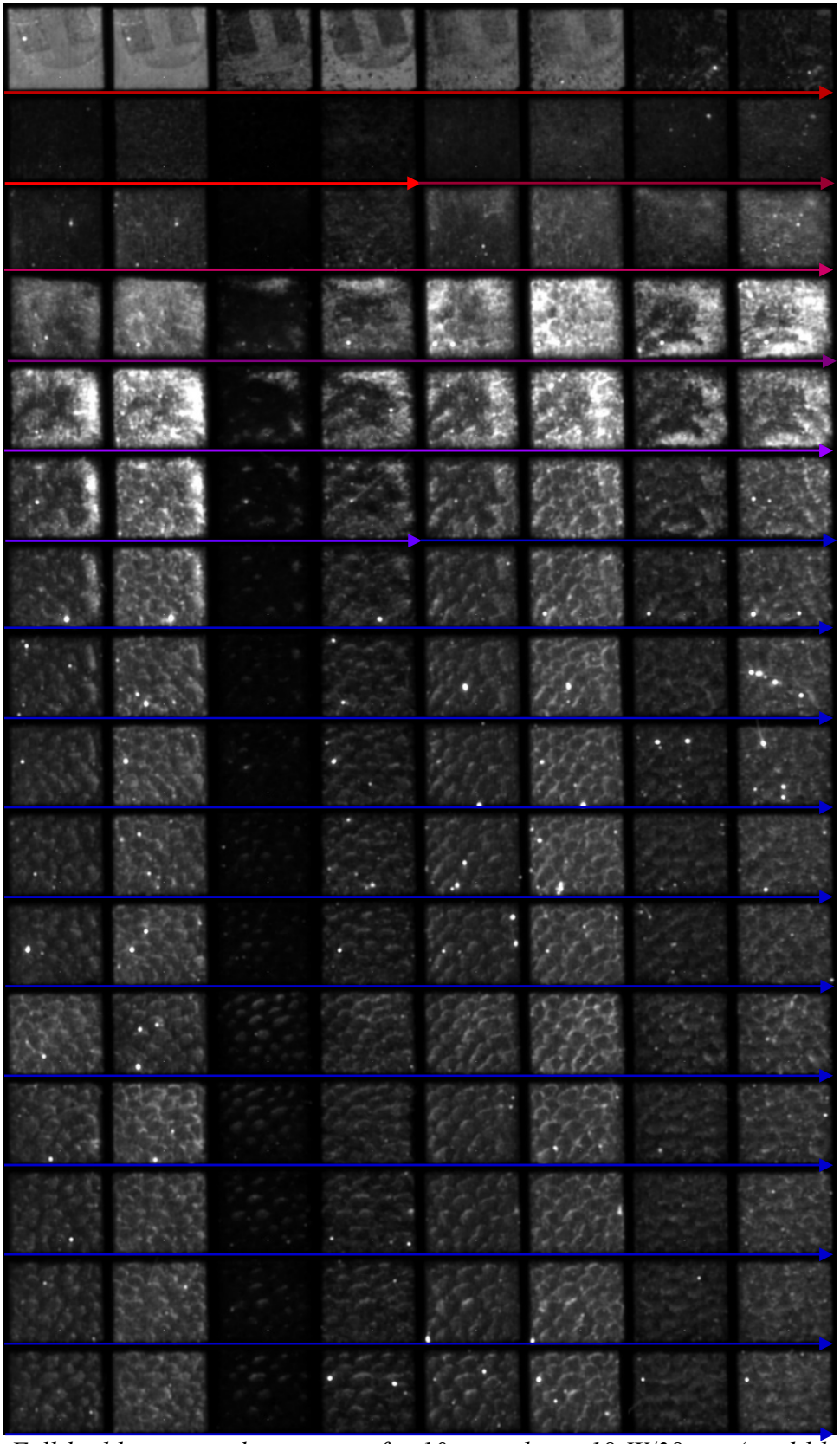

Figure 10: Full build tomography montage for 10mm cube at 18 W/38 µm (read like text, from upper left going horizontally).

Thermal Tomography Data Analysis:

In addition to the visual information, tomography data can be quantified to provide further insights, so the brightness data were analyzed and plotted. An example of the raw tomography data is plotted on the left of Figure 11, with brightness scaled by the 8-bit output. The strong noise component is a manifestation of the 8-cycle scan pattern, and was compensated for with an 8-point sliding average filter. The filter generated a much clearer data set, seen on the right of Figure 11. The data filtering smooths and reduces short term influences on the data, but cycles other than 8 will generate artifacts in the plots, namely brief spikes. Error bars are also included in the right plot of Figure 11, as each brightness value was an average per part. In general, the smaller the error bars, the higher overall part quality was observed, but part-to-part differences across this experiment were minor.

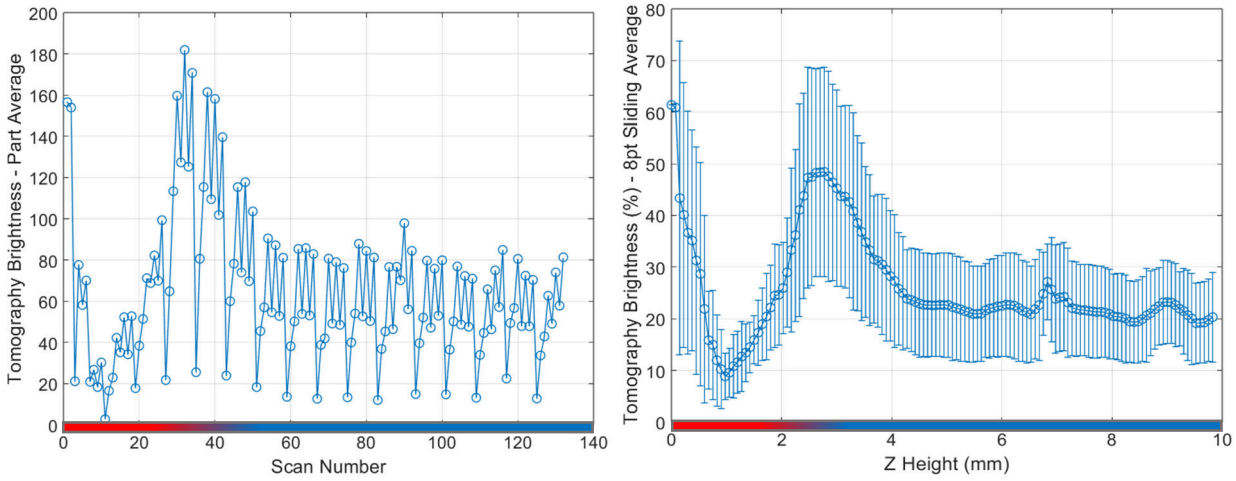

Figure 11: Tomography brightness average per scan of example 3 mm pillar, before (left) and after (right) 8-cycle sliding average filter. The right plot also includes errors bars at plus/minus 1 standard deviation. Note the minor anomalous spike induced at around 7 mm.

Shown in Figure 12 are a pair of similar plots, where the color denotes the same part shapes in both, but the left plot has samples all produced at a lower overall energy input than the right. At the lower energy, the small and large parts end up overlapping after they reach the bulk zone, but the larger amount of overheat shows up readily in the second plot, where the cube remains much brighter.

Part brightness is directly correlated to energy input as expected, but brightness also showed a correlation to the part's scan cross-section, where larger parts were proportionally brighter and consequently hotter. Interestingly, this trend is the opposite of what is expected from structural metals, as smaller parts would usually be hotter due to their reduced ability to conduct away the heat. For thermally insulative bismuth telluride, because the larger parts have a larger ratio of volume to surface area, they are more effective at storing their heat from previous passes, which produces a higher steady state temperature.

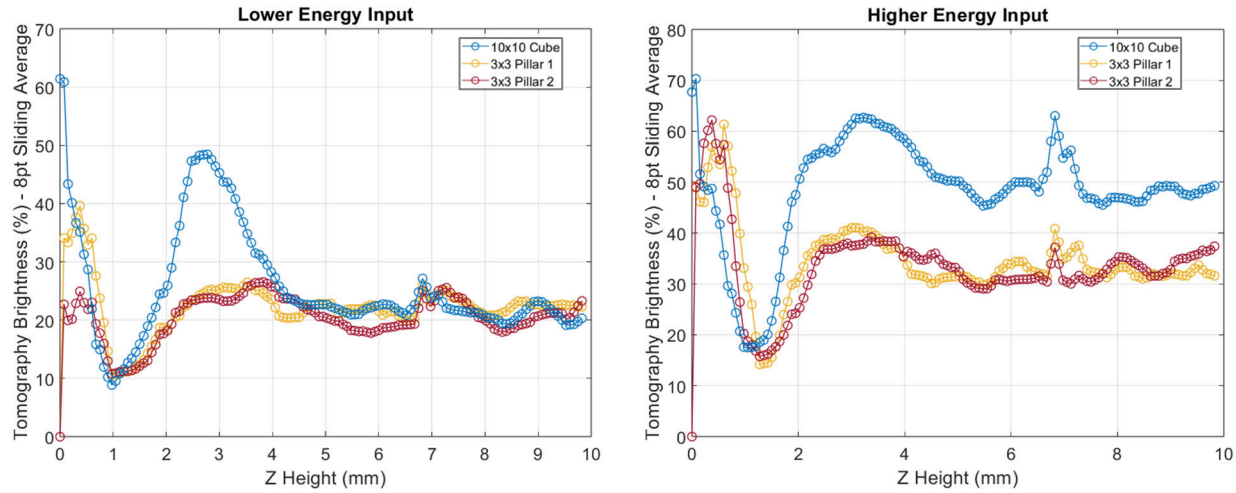

Figure 12: Tomography average brightness plots for various comparative samples at low power (left) and high power (right). Narrow hatch spacing samples are brighter and more distinguishing of part size. Note, as these parts shared a build, the same anomalous spike is induced at around 7 mm.

The left plot of Figure 13 shows the tomography output for the pyramid prints. The two power levels begin at nearly identical brightnesses, but by the bulk region the parts divide into four distinct brightness levels dependent on both power and hatch spacing. There is also a clear downward slope to their bulk regions. The right plot of Figure 13 shows a culminating comparison of the various part cross-sections versus thermal tomography brightness, all produced with the same print parameters.

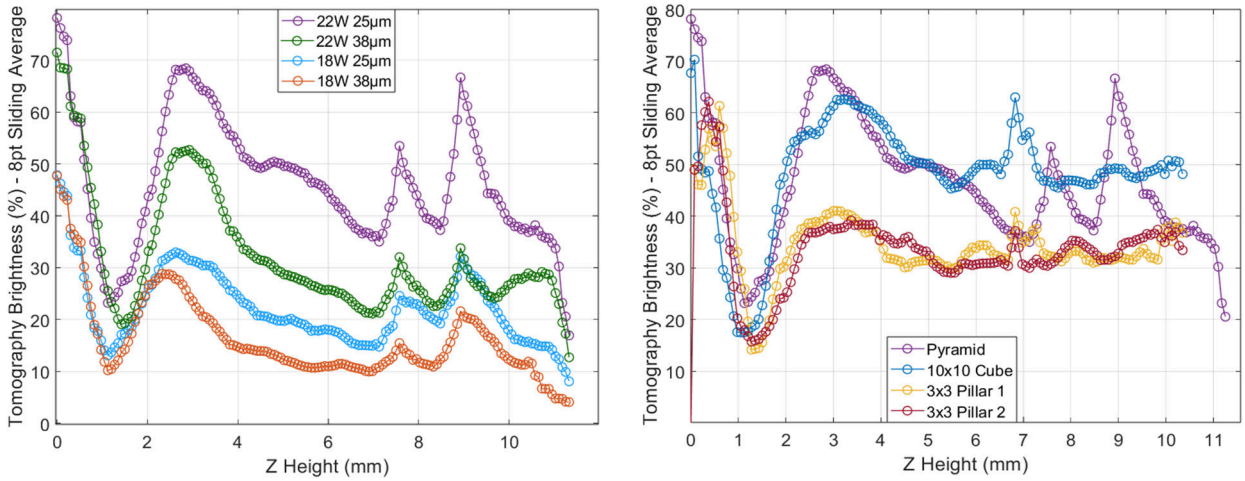

Figure 13: Tomography output for the pyramid samples showing relative brightness decreases(left), and a composite comparison of 3 mm, 10 mm, and pyramid prints at equivalent print parameters (right). Note the pair of anomalous spikes induced in the pyramids at around 7.5 and 9 mm.

Discussion

Advancing Thermal Tomography Process Monitoring:

Thermal tomography imaging shows potential beyond the efforts in this experiment to provide enhanced manufacturing process information. Data from this experiment suggests it is possible to infer certain aspects of print quality from the tomography data by comparing the output against expected thermal buildup, as well as to the statistical spread of brightness across the part. However, in thermoelectric applications where parts are often small and remain within the build plate zone, there will be additional challenges in tomography data interpretation due to the unavoidable build plate interaction. The tomography brightness averages were shown to relate to more than just overall input energy, as they were uniquely modified by the interplay of changing laser power, hatch spacing, and print cross-section. Given enough statistical information, it should be possible to determine all relevant control factors, and to deconvolute each parameter for use in simulation and feedforward applications. By predicting areas with higher heat retention, slicing algorithms can intelligently adjust parameters, ensuring more uniform thermal conditions (a prerequisite for consistent material construction) throughout the build.

More sophisticated analysis of the tomography data is an active area of research [22], and can enable detection of print anomalies such as surface roughness, part delamination, and spatter. The real-time capabilities of the tomography camera offer additional potential for use in feedback control, similar to other commercial thermal sensing solutions. Continuous monitoring of the thermal response can enable real-time adjustments to the print process, immediately addressing detected physical anomalies or off-nominal temperature excursions. This approach has the potential to significantly improve print quality and reduce defects. However, the 'black box' nature of the process control variability and the inability to quantify it for quality control purposes, remains a concern within the industry. Understanding how heat builds up and moves through the part during PBF-LB manufacturing is a critical step in maintaining control of final part quality.

Conclusion

PBF-LB processing has shown potential to revolutionize manufacturing across a multitude of sectors. This research provides a successful proof of concept of the potential to manipulate bismuth telluride at the microstructural level, utilizing varying print parameters, part geometry, and location within the part. These results demonstrated the ability to print different geometric shapes in bismuth telluride, although it remains a challenge to control part tolerances and quality. Increasing the part size was shown to affect microstructure, increasing micro segregation and grain orientation randomness throughout the part.

Using in-situ thermal tomography, certain relational and qualitative aspects of the printing process were elucidated. Similar to other PBF-LB processes, increasing the input energy density will lead to an increase in melt pool temperature and size. But, for bismuth telluride, larger parts at equivalent print parameters will instead be hotter. In addition to the build-long analysis of thermal buildup, it was also shown that per-layer thermal tomography statistics can be used to infer part quality. Qualitative observations of various part attributes were also inferred from the thermal

tomography, including top surface anomalies and part delamination. Further research and understanding will be necessary to control the material at the nanostructural level, with the ultimate goal of being able to directly influence the electronic structure to produce improved thermoelectric performance.

References

[1] H. J. Goldsmid, "The Electrical Conductivity and Thermoelectric Power of Bismuth Telluride," *Proc. Phys. Soc.*, vol. 71, no. 4, pp. 633–646, Apr. 1958, doi: 10.1088/0370-1328/71/4/312.

[2] I. T. Witting *et al.*, "The Thermoelectric Properties of Bismuth Telluride," *Adv. Electron. Mater.*, vol. 5, no. 6, p. 1800904, Jun. 2019, doi: 10.1002/aelm.201800904.

[3] C. B. Satterthwaite and R. W. Ure, "Electrical and Thermal Properties of Bi 2 Te 3," *Phys. Rev.*, vol. 108, no. 5, pp. 1164–1170, Dec. 1957, doi: 10.1103/PhysRev.108.1164.

[4] H. Goldsmid, "Bismuth Telluride and Its Alloys as Materials for Thermoelectric Generation," *Materials*, vol. 7, no. 4, pp. 2577–2592, Mar. 2014, doi: 10.3390/ma7042577.

[5] L. D. Zhao, B.-P. Zhang, J.-F. Li, H. L. Zhang, and W. S. Liu, "Enhanced thermoelectric and mechanical properties in textured n-type Bi2Te3 prepared by spark plasma sintering," *Solid State Sci.*, vol. 10, no. 5, pp. 651–658, May 2008, doi: 10.1016/j.solidstatesciences.2007.10.022.

[6] M. Saleemi, M. S. Toprak, S. Li, M. Johnsson, and M. Muhammed, "Synthesis, processing, and thermoelectric properties of bulk nanostructured bismuth telluride (Bi $_2$ Te $_3$)," *J Mater Chem*, vol. 22, no. 2, pp. 725–730, 2012, doi: 10.1039/C1JM13880D.

[7] F. Kim *et al.*, "3D printing of shape-conformable thermoelectric materials using all-inorganic Bi2Te3-based inks," *Nat. Energy*, vol. 3, no. 4, pp. 301–309, Jan. 2018, doi: 10.1038/s41560-017-0071-2.

[8] M. He, Y. Zhao, B. Wang, Q. Xi, J. Zhou, and Z. Liang, "3D Printing Fabrication of Amorphous Thermoelectric Materials with Ultralow Thermal Conductivity," *Small*, vol. 11, no. 44, pp. 5889–94, 2015, doi: https://doi.org/10.1002/smll.201502153.

[9] Y. Du, J. Chen, Q. Meng, Y. Dou, J. Xu, and S. Z. Shen, "Thermoelectric materials and devices fabricated by additive manufacturing," *Vacuum*, vol. 178, p. 109384, Aug. 2020, doi: 10.1016/j.vacuum.2020.109384.

[10] M. Orrill and S. LeBlanc, "Printed thermoelectric materials and devices: Fabrication techniques, advantages, and challenges," *J. Appl. Polym. Sci.*, vol. 134, no. 3, 2017, doi: 10.1002/app.44256.

[11] C. Oztan, R. Welch, and S. LeBlanc, "Additive Manufacturing of Bulk Thermoelectric Architectures: A Review," *Energies*, vol. 15, no. 9, p. 3121, Apr. 2022, doi: 10.3390/en15093121.

[12] S. L. Sing and W. Y. Yeong, "Laser powder bed fusion for metal additive manufacturing: perspectives on recent developments," *Virtual Phys. Prototyp.*, vol. 15, no. 3, pp. 359–370, Jul. 2020, doi: 10.1080/17452759.2020.1779999.

[13] B. Şişik and S. LeBlanc, "The Influence of Leg Shape on Thermoelectric Performance Under Constant Temperature and Heat Flux Boundary Conditions," *Front. Mater.*, vol. 7, p. 595955, Nov. 2020, doi: 10.3389/fmats.2020.595955.

[14] B. Sağbaş and D. Gürkan, “Investigating compressive strength of laser powder bed fusion manufactured Ti6Al4V lattice structures for bone implant applications,” *J. Addit. Manuf. Technol.*, p. 594 Pages, Dec. 2021, doi: 10.18416/JAMTECH.2111594.
[15] P. A. Hooper, “Melt pool temperature and cooling rates in laser powder bed fusion,” *Addit. Manuf.*, vol. 22, pp. 548–559, Aug. 2018, doi: 10.1016/j.addma.2018.05.032.
[16] C. Wei and L. Li, “Recent progress and scientific challenges in multi-material additive manufacturing via laser-based powder bed fusion,” *Virtual Phys. Prototyp.*, vol. 16, no. 3, pp. 347–371, May 2021, doi: 10.1080/17452759.2021.1928520.
[17] W. Frieden Templeton, S. Hinnebusch, S. T. Strayer, A. C. To, P. C. Pistorius, and S. P. Narra, “A mechanistic explanation of shrinkage porosity in laser powder bed fusion additive manufacturing,” *Acta Mater.*, vol. 266, p. 119632, Mar. 2024, doi: 10.1016/j.actamat.2023.119632.
[18] S. Gao, “Additive manufacturing of alloys with programmable microstructure and properties,” *Nat. Commun.*, 2023.
[19] N. H. Paulson, B. Gould, S. J. Wolff, M. Stan, and A. C. Greco, “Correlations between thermal history and keyhole porosity in laser powder bed fusion,” *Addit. Manuf.*, vol. 34, p. 101213, Aug. 2020, doi: 10.1016/j.addma.2020.101213.
[20] H. Zhang, D. Hobbis, G. S. Nolas, and S. LeBlanc, “Laser additive manufacturing of powdered bismuth telluride,” *J. Mater. Res.*, vol. 33, no. 23, pp. 4031–4039, Dec. 2018, doi: 10.1557/jmr.2018.390.
[21] M. Medale and P. Cerisier, “NUMERICAL SIMULATION OF BE´NARD-MARANGONI CONVECTION IN SMALL ASPECT RATIO CONTAINERS,” *Numer. Heat Transf. Part Appl.*, vol. 42, no. 1–2, pp. 55–72, Jul. 2002, doi: 10.1080/10407780290059422.
[22] A. Agarwal, T. Banerjee, J. Gockel, S. LeBlanc, J. Walker, and J. Middendorf, “Predicting Thermoelectric Power Factor of Bismuth Telluride During Laser Powder Bed Fusion Additive Manufacturing,” Mar. 27, 2023, *arXiv*: arXiv:2303.15663. Accessed: Jun. 28, 2024. [Online]. Available: http://arxiv.org/abs/2303.15663